Fingerprints Indicating Superior Properties of Internal Interfaces in Cu(In,Ga)Se_2 Thin-Film Solar Cells

*Mohit Raghuwanshi, Manjusha Chugh, Giovanna Sozzi, Ana Kanevce, Thomas D. Kühne, Hossein Mirhosseini, Roland Wuerz, and Oana Cojocaru-Mirédin**

Growth of Cu(In,Ga)Se_2 (CIGS) absorbers under Cu-poor conditions gives rise to incorporation of numerous defects into the bulk, whereas the same absorber grown under Cu-rich conditions leads to a stoichiometric bulk with minimum defects. This suggests that CIGS absorbers grown under Cu-rich conditions are more suitable for solar cell applications. However, the CIGS solar cell devices with record efficiencies have all been fabricated under Cu-poor conditions, despite the expectations. Therefore, in the present work, both Cu-poor and Cu-rich CIGS cells are investigated, and the superior properties of the internal interfaces of the Cu-poor CIGS cells, such as the p–n junction and grain boundaries, which always makes them the record-efficiency devices, are shown. More precisely, by employing a correlative microscopy approach, the typical fingerprints for superior properties of internal interfaces necessary for maintaining a lower recombination activity in the cell is discovered. These are a Cu-depleted and Cd-enriched CIGS absorber surface, near the p–n junction, as well as a negative Cu factor ($\Delta\beta$) and high Na content (>1.5 at%) at the grain boundaries. Thus, this work provides key factors governing the device performance (efficiency), which can be considered in the design of next-generation solar cells.

1. Introduction

Cu(In,Ga)Se_2 (CIGS) based thin-film solar cells have now achieved a record efficiency of 23.4%[1] and are one of the most promising alternatives to conventional Si solar cell modules. Manifold attempts have been made over the years to improve the optoelectronic properties of CIGS absorbers by tuning the composition.[2–5] This is because the Cu(In,Ga)Se_2 phase interestingly has a large region of stability on the ternary phase diagram,[6] which extends from a Cu poor region with CGI < 1 (with CGI = [Cu]/([In]+[Ga])) to a stoichiometric region with CGI = 1. This represents the stable α-phase (chalcopyrite "after Beilharz"[6]) of CIGS. Based upon the overall CIGS absorber composition, two types of CIGS absorbers are introduced; that is, Cu-poor CIGS absorber where the overall composition of absorber is less than the stoichiometric value (CGI < 1) and a Cu-rich absorber where the overall composition of the absorber is slightly superior than the stoichiometric value (CGI > 1) and the α-phase is mixed with a Cu_2Se phase. Cu-poor CIGS incorporates numerous defects in the bulk,[7] whereas defects are compensated in Cu-rich CIGS,[8] suggesting that Cu-rich absorbers are more suitable for solar cells.

However, it has been unclear until now why Cu-poor CIGS absorbers are widely used worldwide for obtaining high-performance CIGS solar cells rather than Cu-rich CIGS absorbers.

One important fact is that all the CIGS cells exhibiting world-record efficiencies over the years are comprised of Cu-poor polycrystalline CIGS absorbers,[1,4,5,9–11] (herein called Cu-poor solar cells). Despite their larger grain size, better bulk transport properties, and even better bulk collection efficiency,[8,12–15] Cu-rich CIGS solar cells could never achieve the high efficiency of Cu-poor CIGS solar cells. The main reason were attributed to lower V_{OC} (open circuit voltage) and FF (fill factor) arising due to increased interfacial recombination.[16] More precisely, Turcu et al.[16] have studied the effect of the absorber composition on the recombination mechanism. These numerical calculations have suggested that bulk recombination is dominant in Cu-poor cells, whereas interface recombination is the dominant recombination mechanism in Cu-rich cells. Furthermore, Deprédurand et al.[12] have demonstrated that a higher doping level of the Cu-rich CIGS absorber leads to a very short space charge region width, leading to loss in current and hence

M. Raghuwanshi, O. Cojocaru-Mirédin
RWTH Aachen University
Sommerfeldstraße 14, 52074 Aachen, Germany
E-mail: cojocaru-miredin@physik.rwth-aachen.de

M. Chugh, T. D. Kühne, H. Mirhosseini
Dynamics of Condensed Matter and Center for Sustainable Systems Design
Chair of Theoretical Chemistry
University of Paderborn
33098 Paderborn, Germany

G. Sozzi
Department of Engineering and Architecture
University of Parma
Parco Area delle Scienze 181A, Parma 43124, Italy

A. Kanevce, R. Wuerz
Zentrum für Sonnenenergie- und Wasserstoff-Forschung
Baden-Württemberg
Meitnerstrasse 1, 70563 Stuttgart, Germany

The ORCID identification number(s) for the author(s) of this article can be found under https://doi.org/10.1002/adma.202203954.

DOI: 10.1002/adma.202203954

in efficiency. Recombination at the heterojunction has thus been minimized by forming a Cu-poor surface on a Cu-rich CIGS absorber to exhibit a better charge separation at the p–n junction.[13,17] All of these existing works have tried to improve the performance of Cu-rich CIGS cells, but the Cu-poor CIGS solar cells still prevail in performance.

Recent works have shown that not only the heterojunction, but also the grain boundaries (GBs) in CIGS absorbers play an essential role for the optoelectronic properties of the CIGS-based devices.[18,19] To date, various theories exist explaining the possible benign role of GBs in Cu-poor CIGS absorbers due to the passivation effect induced by alkalis[20–26] or by point defects.[27] However, not much is known about the GB properties of Cu-rich CIGS absorbers, which is essential for enhancing the performance of CIGS solar cells. Couzinie–Devy et al.,[28] have shown that GBs transit from Cu-poor to Cu-rich during the second Cu-rich step of the three stage process, but the electrical properties of these Cu-rich GBs are unknown. Therefore, in this work, we address the chemical and electrical properties of internal interfaces (heterojunction and GBs) for Cu-rich absorbers and compare them with those of Cu-poor absorbers to understand their impact on the cell performance.

For that, temperature-dependent electrical measurements are presented first to understand possible recombination pathways. A detailed analysis of the heterojunction and GBs is described over several length scales by applying correlative atom probe tomography (APT)[29,30] coupled with electron beam induced current studies (EBIC). Correlative APT-EBIC results demonstrate that the heterojunction quality of the Cu-poor cell, characterized by a Cu-depleted absorber surface, is far superior to that of the Cu-rich cell, which is surprisingly characterized by a Se-rich absorber surface observed for the Cu-rich cell. Moreover, a strong correlation between composition and electrical property is observed at the GBs. Namely, the Cu-poor GBs are electrically beneficial, exhibiting an increase in current collection probability, whereas the Cu-rich GBs are electrically detrimental. Two typical fingerprints were discovered for GBs with superior properties, that is, a negative Cu factor ($\Delta\beta$) and a high Na content (>1.5 at%). Experiment-driven density functional theory (DFT) simulations, performed based upon the APT results, confirm that deep gap states are formed for the Cu-rich GBs, which are not completely vanished by decorating the Cu-rich GBs with Na. Last but not least, device simulations are performed and confirm that the Cu-rich GBs (decoration with Cu_{In} defects) in the Cu-rich cells are detrimental for the efficiency of the solar cell, especially for the V_{OC}. In a nutshell, in this work, we attempt to shed light on the role of the internal interfaces in CIGS absorbers, with emphasis on their chemical and electronic properties.

2. Results and Discussion

The Cu-poor sample was grown in a standard three stage CIGS process with CGI = 0.83 (see Experimental Section). The Cu-rich cell was prepared by stopping the CIGS process shortly after the endpoint detection to ensure a Cu-rich composition (CGI = 1.13). As the $Cu_{2-x}Se$ layer on top of this absorber would disturb the CdS growth and destroy the cell completely, we removed this Cu_{2-x} Se top layer by KCN etching and got a CIGS layer with CGI = 0.95 which we further call Cu-rich even though CGI < 1. **Figure 1**a shows the *I–V* curves for the two types of solar cells, with Cu-poor or Cu-rich absorber, and their corresponding electrical parameters. The efficiency of the CIGS solar cell doubles when the overall composition of the absorber is turned from Cu-rich to Cu-poor, within a three stage process, experiencing an increase in V_{OC} of 189 mV, as shown in Figure 1a.

The doubled efficiency for Cu-poor cells stems mainly from a significant improvement in V_{OC} but also from minor improvement in I_{SC} and FF values. The parallel resistance value is astonishingly low for the Cu-rich cells. To look deeper into the performance differences between the Cu-poor and Cu-rich cells, light and dark current–voltage curves were measured at temperatures between 130 and 300 K, as given in Figure 1c,d. The Cu-rich cells have a low parallel resistance, which decreases linearly with decreasing temperature. The *I–V* slope at 0 V is not dependent on light intensity and is the same for the dark and the light curves. In addition, the Cu-rich cells show a light/dark crossover in forward bias, indicating a barrier for the forward electrons, which is removed upon cooling. The Cu-poor cells have no shunts, but the *I–V* curves at low temperatures are S-shaped, indicating a secondary barrier. The deviation from the ideal diode behavior at low temperatures is dependent on illumination intensity, but unlike for Cu-rich cells, it is still present for illuminated devices.

The dependence of the V_{OC} on temperature is shown in Figure 1b. V_{OC} extrapolation to 0 K yields a value of 1200 mV close to the bandgap for the Cu-poor cell, indicating that the dominant recombination mechanism in these devices happens in the bulk. In contrast to the Cu-poor cell, the V_{OC} of the Cu-rich cells extrapolates to 925 mV. The activation energy for the dominant recombination mechanism has a value significantly lower than the bandgap; leading to the conclusion that interface recombination (GBs and p–n junction) is the dominant loss mechanism in the Cu-rich cells. Therefore, in the upcoming three sections, we attempt to explain the origin of the interface recombination in the Cu-rich cells with a special focus on the heterojunction and GBs.

2.1. Heterojunction

Both solar cells, Cu-rich and Cu-poor, are comprised of the same buffer layer (CdS), leading to the same type of heterojunction, namely a p-CIGS/n-CdS junction. The charge carrier generation and collection properties of the n-CdS/p-CIGS junction were investigated using EBIC in the cross section configuration for both cells. **Figure 2** shows the SEM images of the prepared cross section and the corresponding quantitative EBIC maps for the Cu-rich and Cu-poor cells. Since the roughness significantly affects the EBIC results, these cross sections were first cleaned by focused ion beam (FIB). The p–n junction of the Cu-rich cells is clearly visible in the EBIC map due to a clear increase in the EBIC current. No signal from the GBs or lower half of the CIGS absorber layer is observed, in contrast to the case with the Cu-poor cell. This is discussed in more detail in the next section, where GBs are discussed.

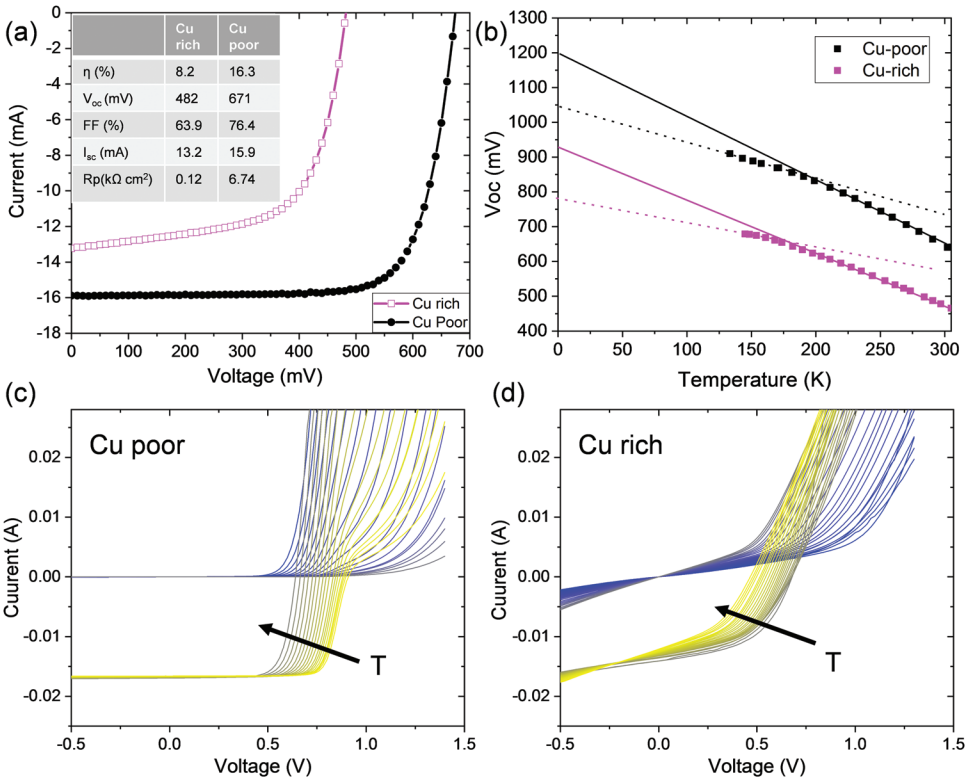

Figure 1. a) *I–V* curves of CIGS solar cells with Cu-rich and Cu-poor compositions. Values of efficiency (η), open circuit voltage (V_{OC}), fill factor (FF), short circuit current (I_{SC}), and parallel resistance (R_p) are shown in the inset in (a) for the two cells. b) Dependence of the open-circuit voltage (V_{OC}) on temperature. c,d) Current–voltage curves for Cu-poor (c) and for Cu-rich (d) cells at different temperatures under dark (blue) and under illuminated (yellow) conditions.

Figure 2c shows the normalized EBIC efficiency profile across the p–n junction and inside the CIGS absorber layer for the Cu-rich and Cu-poor cells. These profiles are extracted from the quantitative EBIC maps obtained at 10 kV and 100 pA. As expected, the maximum EBIC current is observed at the p–n junction for both cells, where the charge carrier separation and collection are at the maximum. However, the collection efficiency for the Cu-poor cells is almost ten times higher than that

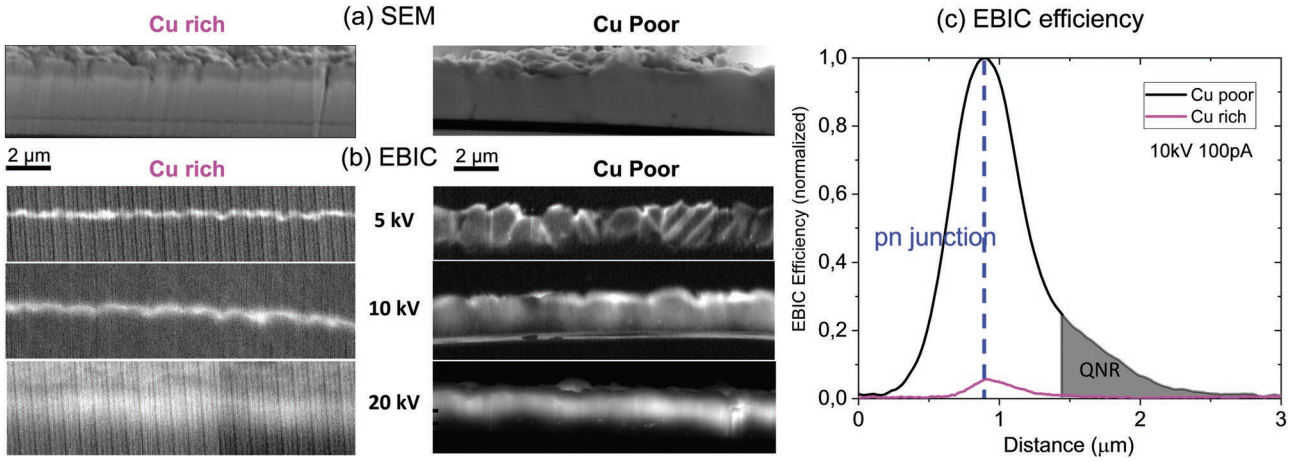

Figure 2. EBIC results for Cu-rich and Cu-poor CIGS solar cells. a) FIB-cleaned cross section as observed in SEM for Cu-rich (left) and Cu-poor (right) CIGS. b) Quantitative EBIC maps acquired on cleaned cross section for Cu-rich and Cu-poor CIGS at different electron beam energies. We note that the regions investigated by EBIC at voltages between 5 and 20 kV are stemming from different places on the sample. This is particularly important to avoid the inclusion of artefacts such as charge carrier generation due to previously imaged conditions and/or possible deposition of carbon contamination (from SEM) on the surface during the image acquisition. Low injection conditions (10 kV, 100 pA) were maintained to avoid high-injection artefacts. c) EBIC efficiency (normalized) for both cells obtained at 10 kV and 100 pA.

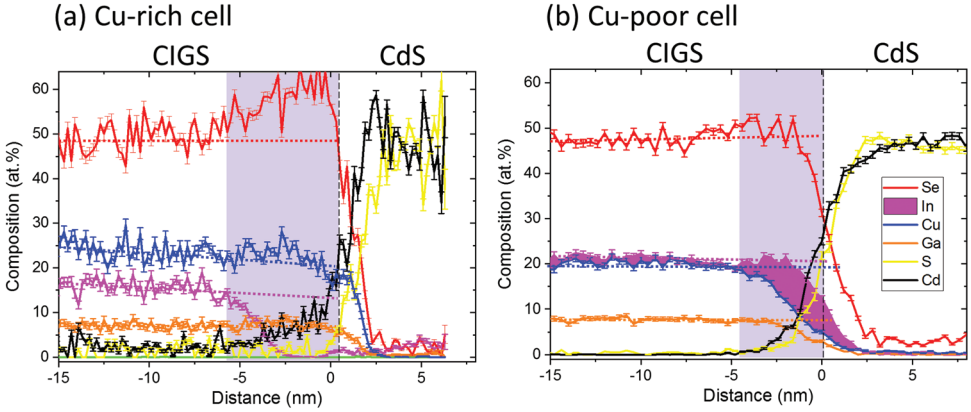

Figure 3. Quantitative APT results of the CdS/CIGS heterointerface and its vicinity. a,b) Composition profiles across heterointerface for Cu-rich (a) and Cu-poor (b) CIGS. The Cu-rich cell shows a strong Se enrichment and In depletion at the CIGS/CdS interface. Possibly, a Se-related defect or a Cd_{In} antisite defect is formed at the heterojunction for the Cu-rich cell. For the Cu-poor cell, a Cu-depleted surface is formed, which promotes the formation of Cd_{Cu} anitsite defects at the interface.

of the Cu-rich cells. These EBIC results raise the question of whether this bold difference in collection efficiency at the p–n junction between Cu-poor and Cu-rich cells is due to peculiar differences in composition.

APT was utilized in this work to probe for the first time the composition of the CdS/CIGS heterointerface in 3D and down to the sub-nanometer level. **Figure 3** shows the proximity histogram, which is basically a composition profile with better statistics (see ref. [31]), of the heterointerface and its vicinity obtained for both Cu-rich (Figure 3a) and Cu-poor (Figure 3b) cells. These two profiles exhibit a striking difference near the heterointerface. The CIGS absorber surface of the Cu-poor CIGS cell is Cu-depleted and In-enriched (see magenta-colored region in violet-colored rectangle), while the CIGS absorber surface of the Cu-rich CIGS cell is Se- and slightly Cu-enriched over a 5 nm depth (see violet-colored region). In fact, the strong Se accumulation (above 60 at%) at the CIGS surface of the Cu-rich cell suggests the formation of a Se-related defect. This is in agreement with the work of Elanzeery et al.,[14] who recently found a Se-related defect at the surface of the Cu-rich absorbers with activation energy of 200 ± 20 meV. They demonstrate that this defect is responsible for the severe heterojunction recombination. In addition, we have identified that this strong Se enrichment at the CIGS surface is accompanied by a strong In depletion (down to 0 at% of In) as well as slight penetration of Cd into the CIGS. This might be a hint for the formation of Cd_{In} defects. On the contrary, the strong Cu depletion at the CIGS absorber surface of the Cu-poor CIGS cell together with the Cd penetration leads to a configuration where Cd_{Cu} defects are formed, pinning the p–n junction and reducing the interface recombination strongly.[32–34]

Furthermore, the device simulation done here on the Cu-rich CIGS cell demonstrates that considering only the recombination coming from the p–n heterojunction cannot reproduce the experimental findings. As given in Figure S1, Supporting Information), for this simulation, a thin 5 nm-thick layer of acceptor-type traps located at 200 meV above the valence band is considered, in agreement with the APT results and ref. [14]. It is clearly shown indeed that the open circuit voltage does not reduce to reach the experimental value of 482 meV, even if the worst-case scenario with a recombination rate of 10^7 cm s^{-1} is considered.

Therefore, even though these findings reveal that the heterojunction in a Cu-rich CIGS cell negatively impacts the cell efficiency, the impact of the GBs on the performance of the CIGS absorber is still unclear. For that, it is necessary to determine the electrical and chemical properties at the GBs together with their band structure and defect states and compare them with the GB properties in a Cu-poor CIGS cell.

2.2. Grain Interior and Grain Boundaries

Before tackling the electrical and chemical properties at GBs, the properties of the grain interior are first investigated, since its properties directly impact the GB properties. It is compelling enough to mention that a significant amount of EBIC current is collected from the quasi-neutral region (QNR) of the CIGS absorber for Cu-poor cells, as shown in Figure 2, yet very negligible contribution of QNR is extracted from the CIGS absorber of the Cu-rich solar cells. Moreover, this very negligible contribution of QNR is stemming mostly from the upper part of the CIGS absorber. This represents an additional evidence that the lower part of Cu-rich thin film consists mostly of inactive grains. The space charge region width is also smaller for Cu-rich cells, in agreement with the work of Deprédurand et al.[12] The diffusion length of electrons for the two samples is estimated based on the different voltages employed to extract the quantitative EBIC profiles from Figure 2 (see Section S2, Supporting Information). The diffusion length for Cu-rich cells is 0.24 µm and is roughly two times smaller than the 0.51 µm of Cu-poor cells. A higher diffusion length indicates better lifetime of carriers, which again demonstrates why Cu-poor cells exhibit a better carrier collection probability. The electron backscatter diffraction (EBSD) maps of the two absorbers (Cu-rich and Cu-poor, see Figure S3, Supporting Information) demonstrate their similar microstructure (grain size and GB distribution). Hence, the difference in microstructure as a possible reason for the stringent difference in cell efficiency, can be disregarded.

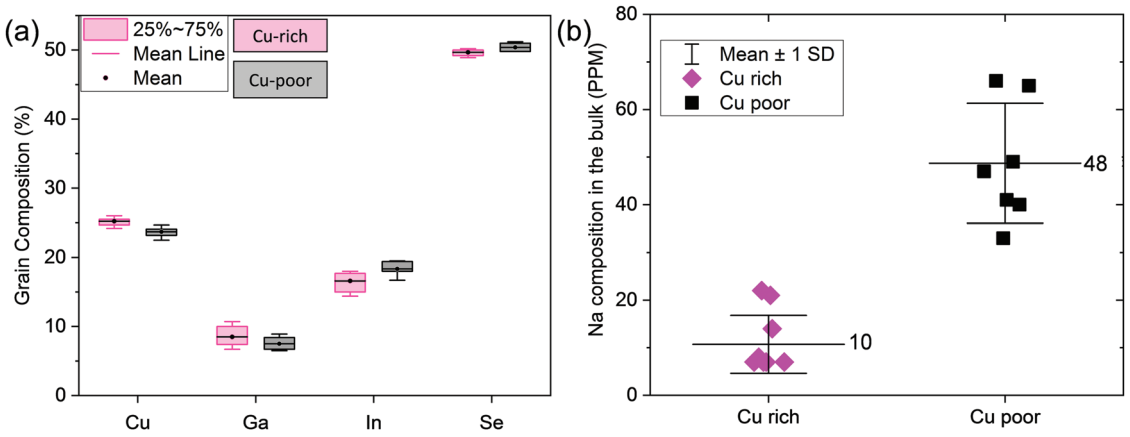

Figure 4. APT investigations of grain interior of CIGS absorber for Cu-rich and Cu-poor cells. a) Composition of the matrix elements (over 15 different grains) for Cu-rich and Cu-poor cells. b) Composition of Na inside the CIGS grains (in ppm) for Cu-rich and Cu-poor CIGS cells. The 7 ppm value given in (b) for the Na content in Cu-rich absorber bulk is in fact a value found below the APT detection limit of 8 ppm, which implies no Na could be clearly identified by APT for those grains. The mean value for the Na composition in each sample is given as well.

Furthermore, it is particularly interesting to highlight the difference in composition of the grain interior (GI) between the Cu-rich and Cu-poor CIGS absorber. **Figure 4**a shows the average matrix composition measured for the two samples. More than 15 grains have been measured for each sample, that is, Cu-poor and Cu-rich CIGS. The mean value of Cu in Cu-rich CIGS is just above stoichiometric value at 25.2 at% Cu, while that of Cu-poor CIGS is 23.8 at% Cu. It is obvious that the mean value of In+Ga composition in the grain interior for the Cu-rich cell is slightly lower (25.2 ± 0.7 at%) than that for the Cu-poor cell (25.9 ± 0.7 at%) due to the 50:50 stoichiometry requirement. Interestingly, the Se content in the grain of the Cu-rich CIGS absorber is ≈0.5 at% (± 0.5 at%) lower than that for the Cu-poor CIGS absorber. This corroborates well with the findings from Figure 3a, where a Se accumulation at the CIGS surface is observed, suggesting that Se-related defect formation at the CIGS surface leads to a reduced overall Se content inside the CIGS absorber for the Cu-rich cell.

Contrary to the matrix elements, the Na dopants were not introduced in the absorber in a controlled way, such as via post-deposition treatment. Rather, Na diffused from the soda lime glass substrate during the processing. It is important to mention here that the APT detection limit of Na inside CIGS is as low as 8 ppm, which makes it a highly effective tool for detailed analysis of Na dopants. Figure 4b shows the Na composition inside the CIGS grains of Cu-rich and Cu-poor CIGS cells. It is striking that the overall Na composition inside the grains is almost five times higher for Cu-poor CIGS (48 ± 12 ppm) than for Cu-rich CIGS (10 ± 5 ppm).

Zhang et al.[27] have demonstrated that the Cu vacancies (V_{Cu}) are the defects with the lowest formation energy in Cu-poor CIGS, whereas the Cu_{In} antisites are the defects with the lowest formation energy in Cu-rich CIGS. Moreover, it is now well established that Na atoms occupy Cu vacancies.[35] Therefore, the high amount of Cu vacancies in Cu-poor CIGS facilitates the insertion of a higher amount of Na, explaining the large discrepancy in Na content between Cu-poor and Cu-rich CIGS absorbers. Thus, our results are in good agreement with theoretical predictions that show higher Na levels for Cu-poor grains.[35]

GBs have been intensively studied for Cu-poor CIGS systems by various groups, and a recent comprehensive review summarizing all existing works can be found in ref. [19]. However, no publication exists yet on GBs in Cu-rich CIGS absorbers. Therefore, in this section, we present the electrical and chemical properties of these GBs in comparison with the GBs of the traditional Cu-poor CIGS absorber and we connect these findings to the band structure.

The quantitative EBIC cross-section images from Figure 2 reveal the position of the GBs in the Cu-poor CIGS absorber, but no contrast is observed for the GBs in the Cu-rich absorber. This can be explained only by two possible reasons. The first explanation is that there are no GBs. This hypothesis can be excluded, since Figure S3, Supporting Information, clearly shows an average grain size of 0.6 µm. The second and the only plausible explanation is that the GBs trap the electrons and prevent them from reaching the CdS (n-type) layer. These observations are contradictory to the observations made for the GBs in Cu-poor cells, that is, the GBs are active throughout the entire CIGS thin film, as shown in Figure 2b. Especially at low injection conditions (5 kV voltage and 100 pA current), the charge carrier separation is very effective and even enhanced. This is in agreement with previous results obtained for CIGS and CdTe solar cells,[23,36–38] where an enhanced carrier collection from GBs is typically observed.

EBIC measurements were also performed on the CIGS surface to better map the electrical properties of GBs for both Cu-rich and Cu-poor CIGS absorbers, applying the procedure described in refs. [18,39]. The quantitative EBIC maps obtained are shown in **Figure 5**. Higher brightness here corresponds to a better collection of charge carriers and vice versa. It is evident that the charge collection dynamics significantly differs between the Cu-rich and Cu-poor cells. For Cu-poor CIGS, we can clearly see that some GBs are dark and hence electrically detrimental, while many of them are bright and thus considered electrically beneficial. These GBs are even more visible on the EBIC map when using lower energy electrons (5 kV), which is a result of the smaller penetration depth. At higher beam energy (10 kV or higher), the penetration depth of the

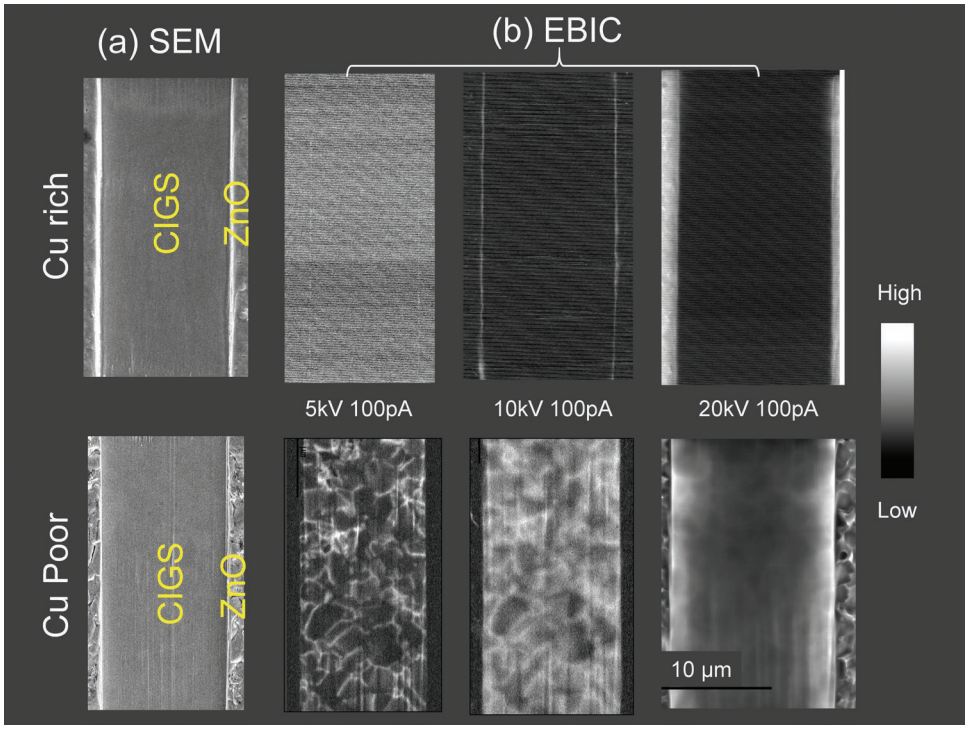

Figure 5. Surface EBIC measurements for Cu-rich and Cu-poor absorbers. a) SEM and b) corresponding surface EBIC maps of Cu-rich (top) and Cu-poor (bottom) CIGS solar cells. The middle part corresponds to exposed CIGS upon FIB cleaning, and left and right parts contain the ZnO and CdS (found below ZnO) layer. The current values in the EBIC maps are normalized.

electrons is significantly larger, hence the EBIC signal at GBs is averaged with the one coming from the corresponding grains. Moreover, the signal further faints at the GBs because of their increased tilting angle within the absorber depth. In correlation with the results obtained by EBSD, many neutral boundaries (with no relative change in EBIC) are also observed, as shown in Figure S4, Supporting Information. However, for Cu-rich CIGS, only the p–n junctions on the sides of the trenches display an enhanced EBIC signal at 5 kV (faintly visible) and 10 kV (clearly visible). No change in EBIC contrast is observed at the GBs for Cu-rich samples, which exhibit a striking difference in electron collection probability at the GBs when compared to the Cu-poor CIGS absorber.

Particularly interesting here is to understand if this dramatic change in electrical properties is accompanied by composition changes as well. **Figure 6** shows the 3D APT maps for Cu-rich and Cu-poor absorbers, where the atomic distribution of Na and Se atoms as well as the 3D Cu composition maps are given. It is evident that the planar segregation of Na marks the position of the GBs. This correlates precisely with the Cu composition changes observed in the 3D composition maps. These results highlight two distinct behaviors. The GBs of the Cu-rich CIGS absorber show a systematic Cu enrichment, while the GBs of the Cu-poor CIGS absorber exhibit an opposite Cu behavior, that is, Cu is depleted. This Cu enrichment or Cu depletion is very confined (≈2 nm) and homogenous over the entire portion of the GB, which excludes any possibility of unwanted clustering (early stage for phase formation, such as $Cu_{2-x}Se$ phase) that might be detrimental for solar cell performance.

Figure 7 gives the same information as Figure 6, but in a more quantitative manner. More precisely, Figure 7 shows the

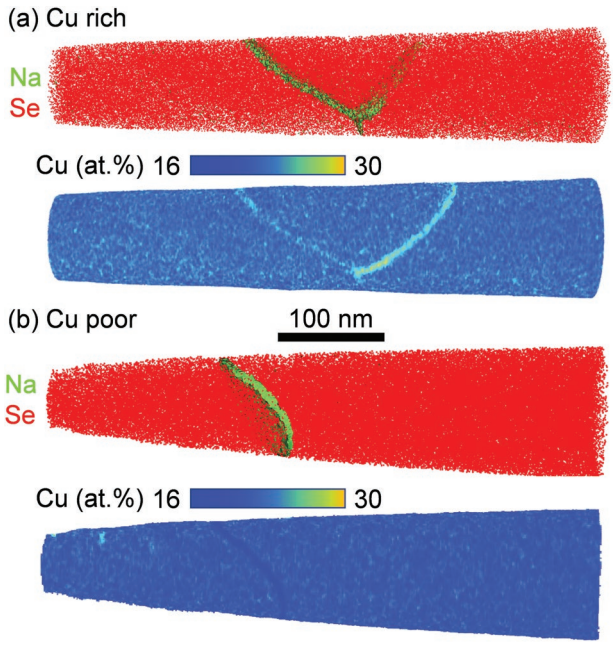

Figure 6. 3D APT map of GBs in Cu-poor and Cu-rich CIGS absorber. a,b) 3D atomic distribution maps of Na and Se mark the location of the GBs, while the 3D Cu composition maps indicate Cu enrichment for Cu-rich CIGS absorber (a) and Cu depletion for Cu-poor CIGS absorber (b).

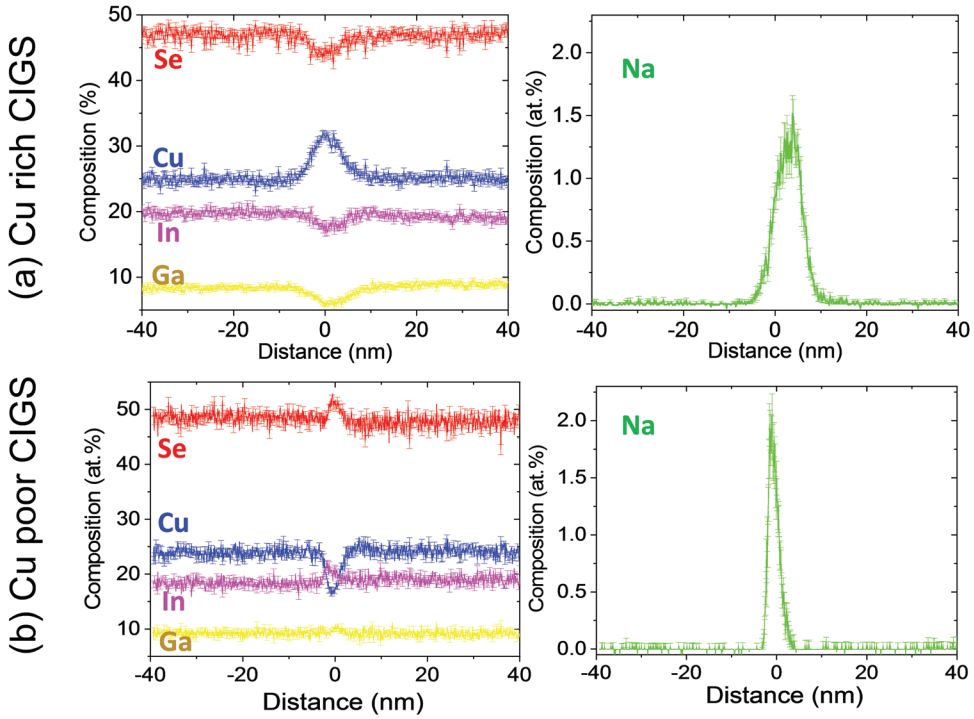

Figure 7. 1D APT linear composition profiles at GBs of matrix elements and Na dopant. These 1D composition profiles are extracted from the 3D maps from Figure 6 showing the contrasting results between the two samples, namely the GB of the Cu-rich absorber is Cu-enriched and In-depleted, while the GB of the Cu-poor absorber is Cu-depleted and In-enriched. The Cu-rich GB contains a lower Na content (≈1.3 at%) than the Cu-poor GB (≈2.0 at%).

1D composition profiles of all matrix elements found inside the CIGS absorber as well as of Na dopants segregated at the GB. The GB in the Cu-rich CIGS absorber is Cu-enriched by ≈+5.2 at%, while the In, Ga, and Se are depleted (ΔIn = −3.0, ΔGa = −2.1, ΔSe = −1.1), as shown in Figure 7a. Moreover, Na is segregated at this specific GB by ≈1.1 at%. In contrast, the GBs of the Cu-poor CIGS absorber is Cu-depleted by ≈−8 at%, while the In and Se are enriched (ΔIn = +3.8, ΔSe = +2.9), as shown in Figure 7b. Another difference observed is that for the Cu-poor GB, Na exhibits a stronger segregation of up to 2 at%. These results are shown for one typical GB from each respective CIGS absorber. However, previous works have shown that GBs with multiple compositions can coexist in the same CIGS material.[18,40–44] Hence, further investigations were performed on many other GBs to obtain a larger data sample for a better comparison.

Table 1 shows the composition of the matrix elements as well as of the Na and O contents measured for all GBs analyzed for the Cu-rich and Cu-poor CIGS absorbers. Cu-poor GBs in the Cu-poor cells have a similar composition among themselves that coincides remarkably with the GB composition observed for record-efficient cells.[34] Based on the correlative EBIC-APT investigations, these Cu-poor GBs detected in the Cu-poor CIGS cell are electrically beneficial and represent the vast majority of the GBs (58%). Moreover, these GBs exhibit a pronounced Cu depletion (≈ −8 at%) accompanied by Se and In enrichment (≈ +3 at% and +3 at%, respectively). This indicates that these Cu-poor GBs are mainly dominated by donor-type defects such as In_{Cu} and Se_{Cu}, in good agreement with the work of Gaury et al.[45] They predicted indeed that a single donor state at GB would result in GB recombination comparable to that of the bulk. Furthermore, the average Na content segregated at the GB is of about 2 at%. It is important to note that electrically detrimental GBs have been also detected by EBIC in a Cu-poor absorber and measured by APT, but they represent only a minor proportion of GBs in CIGS (15%). Surprisingly, they exhibit mostly a Cu enrichment and In depletion behavior. These electrically detrimental GBs exhibit no or very little Na content and are sometimes accompanied by O accumulation.

Correlative EBIC-APT analysis could not be carried out on the GBs in the Cu-rich absorber, since these GBs do not display any EBIC contrast changes. Hence, these GBs and grains were investigated randomly. Table 1 summarizes the composition of nine GBs investigated. It is thrilling to see that all the GBs exhibit similar composition, that is, Cu is always enriched while Se, In, and Ga are depleted, and recall the behavior of the Cu-rich GBs in the Cu-poor cell. One common feature of both Cu-rich and Cu-poor CIGS absorbers is that the Σ3 twin boundaries do not show any change in composition and no dopant (Na) or impurity (O) segregation, in agreement with previous works.[44,46] Moreover, random high-angle GBs with their respective disorientation angles ranging from 22° to 58.1° do not show any appreciable correlation between the GB angle and the amount of Na segregation detected by APT.

It is worthwhile to mention here that the composition of the GBs for both Cu-rich and Cu-poor cells is closely related to the respective bulk composition. Very surprisingly the behavior of Cu and In cations in the grain perfectly mimics the behavior of cations at the neighboring GB for both cells due to stoichiometry imposition. More precisely, a Cu-rich, In-poor grain

Table 1. Composition of GBs determined by APT in Cu-rich and Cu-poor CIGS absorbers. For the Cu-poor CIGS absorber, the white-colored section includes the electrically neutral GBs (which represent the Σ3 twin boundaries, [TBs]), the green-colored section includes the electrically beneficial GBs, while the pink-colored region provides the electrically detrimental GBs. For the Cu-rich CIGS absorber, the orange-colored section includes all GBs investigated, where most of them are random high-angle GBs and one GB is a Σ3 TB. Here, Δ = (composition at GB) − (composition in GI).

	GB disorientation angle	Na [at%]	O [at%]	ΔCu [at%]	ΔSe [at%]	ΔIn [at%]	ΔGa [at%]
Cu-rich CIGS	37.4°	0.5	0	+3.5	−2.5	−1.4	−1.2
	23.1°	1.5	0	+6.8	−4.6	−2.7	−3.0
	50.8°	0.9	0	+3.9	0	−2.8	12.2
	45.2°	1.1	0	+5.2	−1.1	−3.0	−2.1
	49.1°	0.3	0	+4.1	−1.5	−2.2	−1.4
	58.1°	0.4	0	+4.0	−2.1	−1.3	−1.0
	22°	0.2	0	+2.7	0	−1.6	−1.3
	43°	0.3	0	+3.6	−1.8	−0.6	−2.1
	60°(Σ3)	0	0	0	0	0	0
Cu-poor CIGS	60°(Σ3)	0	0	0	0	0	0
	60°(Σ3)	0	0	0	0	0	0
	60°(Σ3)	0	0	0	0	0	0
	81°	2	0	−8.0	+3.8	+2.9	0
	46.5°	1.7	0	−7.8	+3.0	+3.0	0
	21.8°	2.5	0	−9.3	+4	+3.5	0
	24°	0	0	+3.5	−2.0	−1.5	0
	88°	0.4	0.6	+4.5	−1.7	0	−3.5
	22.2°	0.1	0.3	+2.5	−1.3	+4.2	−5.4

in a Cu-rich CIGS absorber results in a Cu-rich, In-poor GB. The reverse holds true: a Cu-poor, In-rich grain in a Cu-poor CIGS absorber results in a Cu-poor, In-rich GB in most cases. In fact, the Cu in the grain is pushed out to maintain the stoichiometric ratio (25:25) during the growth of the CIGS under Cu-rich conditions. Therefore, all the Cu surplus is moved to the GBs, explaining why the Cu-rich CIGS contains Cu-rich GBs. However, during the third stage of the growth, Ga and In diffuse into the Cu-rich layer and convert it into a Cu-poor layer, so a high proportion of Cu vacancies can be easily accommodated under these circumstances. Depending on the quality of the third stage, more or fewer GBs with Cu enrichment are left. Concerning the Se anions, a higher Se content at the CIGS surface and at the GBs in the Cu-rich cell directly converts to a lower Se content in the grain and vice versa. Thus, by determining the composition of the grains, we can predict with high probability the composition of their respective neighboring GBs.

Recently, we have implemented a parameter called the Cu factor ($\Delta\beta$),[19] which is defined as the difference in composition changes (Δ = (composition at GB) − (composition in GI)) at a GB between Cu and Se + In + Ga:

$$\Delta\beta = \Delta\mathrm{Cu} - (\Delta\mathrm{Se} + \Delta\mathrm{In} + \Delta\mathrm{Ga}) \quad (1)$$

This Cu factor is an attempt to mimic the charge defect available at the GB region. More precisely, acceptor-type defects are preferentially present in Cu-rich GBs (Cu_{Se}, Cu_{In}, and Cu_{Ga}), while donor-type defects are preferentially present in Cu-poor GBs (In_{Cu}, Ga_{Cu}, and Se_{Cu}). Hence, a positive value *of* $\Delta\beta$ suggests that acceptor-type defects are preferentially present at the GB, while a negative value *of* $\Delta\beta$ suggests that donor-type defects are preferentially present at the GB.

The Cu factor values for Cu-rich and Cu-poor samples are plotted in **Figure 8**. Figure 8a shows the Cu factor calculated at the GBs as a function of their respective EBIC signal for the Cu-poor cell. A remarkable correlation between the composition and the EBIC current at the GB is observed. The Cu-poor GBs that are electrically beneficial exhibit a strong negative value for $\Delta\beta$. On the other hand, the Cu-rich GBs that are electrically detrimental exhibit a strong positive $\Delta\beta$ value, while the $\Delta\beta$ value for the electrically neutral GB stays zero. In the case of the Cu-rich absorber, the GBs were not visible in the EBIC analysis, hence the change in EBIC at the GBs could not be evaluated. However, the $\Delta\beta$ values calculated for the GBs are all positive, ranging between 6 and 12, as shown in Figure 8b. By comparing the $\Delta\beta$ values of the GBs in Cu-rich CIGS (Figure 8b) with the GBs from the red region of Figure 8a, we can conclude that all the GBs in Cu-rich CIGS are electrically detrimental being characterized by a positive $\Delta\beta$ value. This indicates that the defect chemistry of GBs in Cu-rich CIGS differs completely from that of the majority of GBs in Cu-poor CIGS (some of them being represented in the green region of Figure 8a). As mentioned above, a positive $\Delta\beta$ value indicates formation of Cu_{In} acceptor-type defects at GBs in Cu-rich CIGS. In contrast, a negative $\Delta\beta$ value indicates formation of In_{Cu} donor-type defects at GBs in Cu-poor CIGS.[47]

Not only the Cu factor ($\Delta\beta$) is a fingerprint by which we can identify GBs with superior properties, but also the level of Na segregation. Figure 8a shows that the Na content is higher

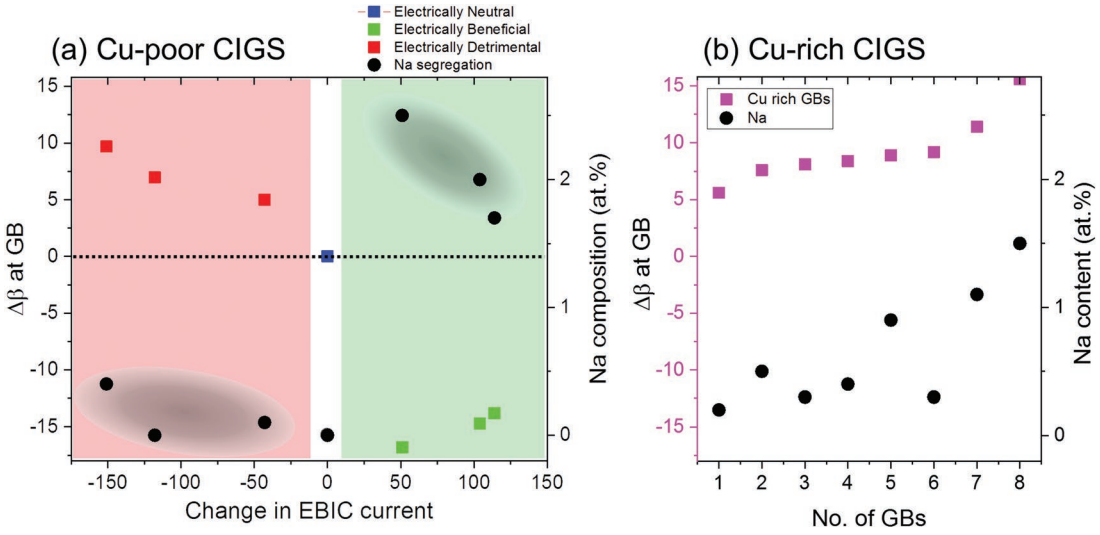

Figure 8. Fingerprints of GBs with superior properties. a) Cu factor ($\Delta\beta = \Delta Cu - (\Delta Se + \Delta In + \Delta Ga)$) is represented versus the change in EBIC current at GBs of Cu-poor CIGS. The Na content for the respective GBs is given as black dots, clearly revealing two regions, that is, 1) low Na content for GBs with positive $\Delta\beta$ and 2) high Na content for GBs with negative $\Delta\beta$. b) Cu factor for Cu-rich CIGS. No EBIC information is available, but only positive $\Delta\beta$ values and low Na contents are observed. By extrapolating with the results from (a), we conclude that GBs in the Cu-rich cell do not fulfill the fingerprints necessary for superior GB properties, that is, negative $\Delta\beta$ values and high Na content (>1.5 at%).

than 1.5 at% for all electrically beneficial GBs (Cu-poor GBs), while it is below 0.5 at% for electrically detrimental ones. The average Na content at GBs in Cu-rich CIGS (Figure 8b) is 0.65 at%, which is in the vicinity of the contents of electrically detrimental GBs. Thus, Figure 8 suggests that Cu-rich GBs found either in Cu-poor CIGS or in Cu-rich CIGS exhibit both fingerprints for deteriorated properties of the GBs, that is, positive $\Delta\beta$ values and low Na content.

Correlative EBIC-APT investigations suggest that Cu-poor and Cu-rich GBs differ in the type of defect present, that is, Cu-poor GBs are dominated by (V_{Cu} + In_{Cu}) defects while Cu-rich GBs are dominated by (Cu_i + Cu_{In}) defects. To consolidate this finding, experiment-driven DFT simulations were performed to gain a deeper insight into the defect states created by GBs. For simplicity, we considered a more simple twin boundary (TB) model based on two (114) surfaces according to Chugh et al.[48] Voids, dangling bonds, and wrong bonds that occur in this TB model make it appropriate for studying random GBs. To make GB regions Cu-rich or Cu-poor, ($2Cu_i$ + Cu_{In}) and ($4V_{Cu}$ + $2In_{Cu}$) defects have been introduced into the GB models, respectively. The corresponding atomic structures are shown in **Figure 9**. When the GB region is Cu-rich, deep gap states are observed (see Figure 9a), even when Na is present (Figure 9c). It is known that the deep gap states present at GBs can act as recombination centers.[49] On the other hand, when the GB region is Cu-poor (see Figure 9b), narrow gap states close to the valence band maximum and conduction band minimum are observed. Interestingly, these gap states are not vanished but only slightly diminished by inserting Na dopants at the GB region (see Figure 9d). The relative shift of the band edges for Cu-rich and Cu-poor GBs indicated that both GB models shift the valence band maximum to a lower energy level. That means that the region next to a GB is depleted of holes. Therefore, these experiment-driven DFT calculations demonstrate that a Cu-poor GB configuration is more favorable for the electron transfer than a Cu-rich GB configuration due to the reduced recombination activity (absence of deep gap states and wider bandgap, in contrast to Cu-rich GB) in addition to the hole depletion near the GB region.

Although the EBIC results together with the DFT simulations indicate that Cu-rich GBs are not as well-suited for charge transport as the Cu-poor GBs, it is not clear up to this point what the real impact of these Cu-rich and Cu-poor GBs is on the conversion efficiency of the entire cell. To reveal that, device simulations were performed on a CIGS solar cell containing either Cu-rich GBs or Cu-poor GBs and compared with a device containing no GB. The results obtained are summarized in **Table 2**. We note here that details about these device simulations can be found in Experimental section.

The bandgap (E_g) values provided for both bulk (or grain interior, GI) and GB are calculated based on the methodology described in ref. [3], which relies mostly on the APT composition values. The bandgap obtained for the Cu-rich GBs is 100 meV smaller than the bandgap of the bulk, which leads to a negative valence-band or conduction-band offset, as simulated by samples B′ and C′. In contrast, the bandgap obtained for Cu-poor GBs in Cu-poor cells is 110 meV larger than the bandgap of the bulk, which leads to a positive valence-band or conduction-band offset, as simulated by samples B or C in Table 2. Sample A′ or A corresponds to a CIGS solar cell where the bandgap of the GBs is similar to that of the bulk material, that is, no band offset. Moreover, based on the DFT calculations, a shallow-acceptor Cu_{In}/Cu_{Ga} localized at $E_V + 0.1$ eV and a deep level at $E_V + 0.6$ eV are introduced for the Cu-rich GB, whereas only a shallow-donor In_{Cu} energy level localized at E_C–0.05 eV is introduced for the Cu-poor GB.[45] We note here that the density of these charged defects is increased at the GB region ($\approx 5 \times 10^{18}$ cm^{-3}) when compared with the bulk region (10^{14} cm^{-3} in Cu-rich cell and 3.5×10^{15} cm^{-3} in Cu-poor cell).

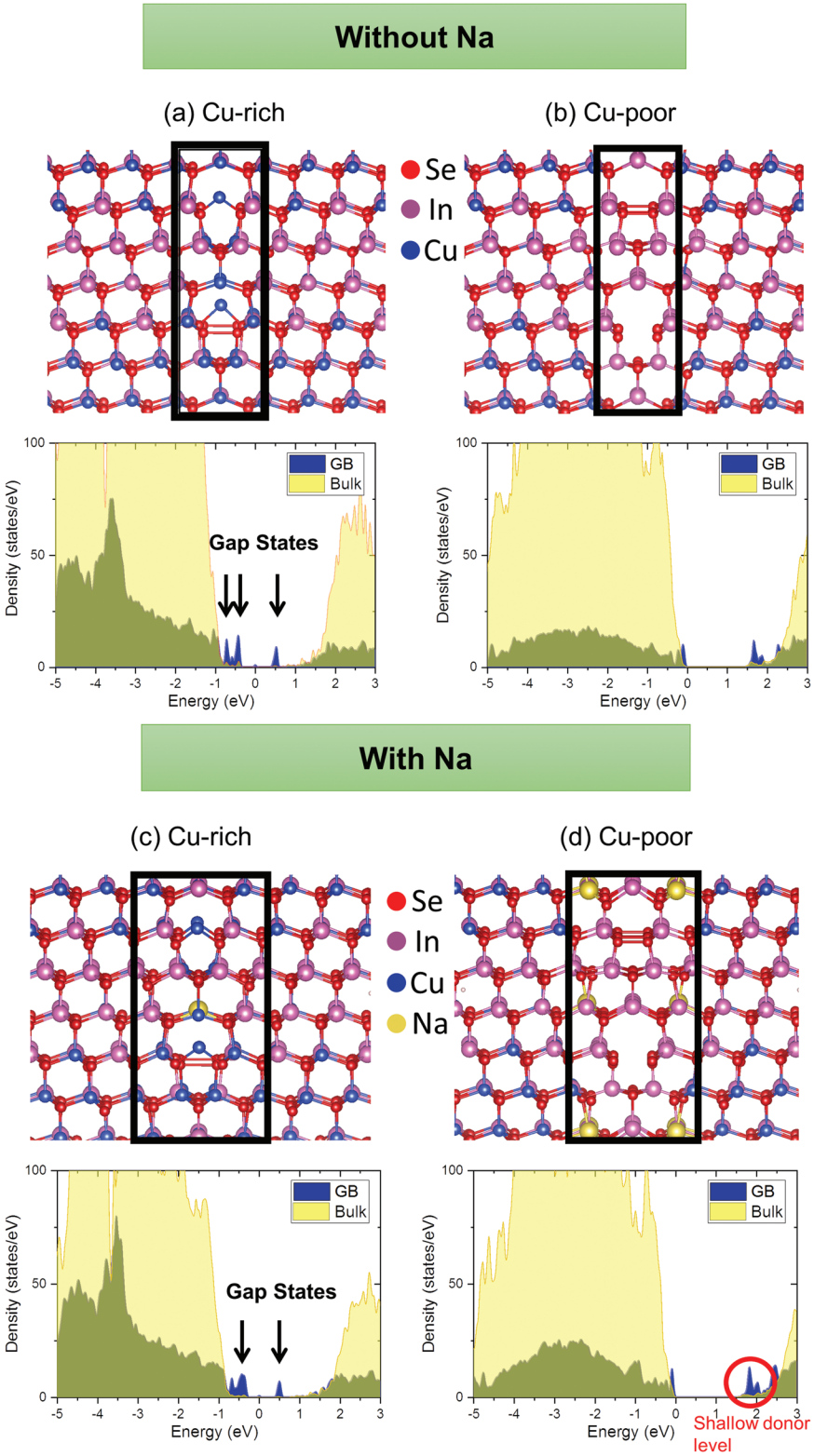

Figure 9. DFT calculations for the Cu-rich and Cu-poor GBs without and with Na doping. a–d) Atomic structure of the Σ3(114) GB and calculated density of states for Cu-rich (a,c) and Cu-poor (b,d) CIGS. It is important to mention that only the regions next to GBs are Cu-poor/Cu-rich. The rest of cell is stoichiometric. In fact, the stoichiometric "bulk" region is kept as a reference for band alignment calculations.

Since no carrier concentration at GB or GI has been measured on these devices until now, the effect has been studied by numerical simulations (see Section S5, Supporting Information). Results show that reducing or increasing the p-type doping of GB compared to the grain interior of one order of magnitude has very little effect on both the band bending

Table 2. CIGS device simulation containing either Cu-poor or Cu-rich GBs. The cell parameters (such as open circuit voltage (V_{OC}), short circuit current density (J_{SC}), fill factor (FF), and efficiency (η)) obtained from simulation are compared with the experimental ones.

			E_g [eV]						
		Sample	GI	GB	GI–GB interface $\Delta E_c/\Delta E_v$ [meV]	V_{OC} [mV]	J_{SC} [mA cm^{-2}]	FF [%]	η [%]
Cu-rich GB	Experiment	–	–	–	–	482	26.5	63.9	8.16
	Simulation: No GB		1.2	–	–	772	33.18	84.43	21.66
	Simulation: with GB	A′	1.2	1.2	0/0	590	28.29	67.19	11.21
		B′	1.2	1.1	0/100	512	26.72	64.09	8.76
		C′	1.2	1.1	100/0	514	26.51	63.97	8.72
Cu-poor GB	Experiment	–	–	–	–	671	31.9	75.90	16.2
	Simulation: No GB		1.18	–	–	741	33.38	78.42	19.39
	Simulation: with GB	A	1.18	1.18	0/0	637	30.96	77.27	15.23
		B	1.18	1.29	0/110	670	31.99	75.90	16.26
		C	1.18	1.29	110/0	665	31.44	76.27	15.94

and cell behavior (Figure S5 and Table S1, Supporting Information), because of the large density of defects considered at the GB. Yet, a minor effect is noticeable in the case of Cu-rich cell, where the largest p-type GB doping raises the band bending of about 4 meV and the cell efficiency of about 1.2% relative (Figure S6 and Table S2, Supporting Information), mainly due to a reduced recombination at the GB.

These device simulations provide already a robust understanding of the impact of Cu-rich or Cu-poor GBs on the performance of their respective devices. The Cu-rich GBs that are electrically detrimental as observed by EBIC are also detrimental for the cell performance, especially for the V_{OC} (sample B′ and C′). This is mainly due to the 100 meV decrease in bandgap at the GB leading inherently to an increase in recombination activity. Interestingly, the presence of a Cu-poor GB by itself (sample A), with no band offset and containing a high density of donor defects, is detrimental for cell performance, especially for the V_{OC}. However, the V_{OC} value improves when a small band offset of only 110 meV is present at the GB (sample B or C). Both effects, the bandgap increase and valence-band bending, taking place at the Cu-poor GB lead to a drastic decrease in recombination activity, thus explaining the increase in EBIC current observed at Cu-poor GBs (Figure 5). Therefore, these device simulations confirm that the electrically beneficial Cu-poor GBs detected by EBIC are favorable for electron collection and conductivity and hence are not that harmful for the overall cell performance. However, the electrically detrimental Cu-rich GBs are characterized by an increased charge recombination and thus are detrimental for the device performance, especially for the V_{OC}.

3. Conclusion

We have considered the case of a Cu-rich and a Cu-poor CIGS solar cell to investigate the typical fingerprints for superior properties of internal interfaces necessary for achieving a high-performance CIGS thin-film solar cell. The efficiency of a Cu-poor cell (<25% Cu) becomes half after it is made Cu-rich (>25% Cu), which is explained by the dominant interface

recombination, as shown by the temperature-dependent V_{OC} measurements. EBIC measurements consolidated this finding by showing reduced collection probability at both the p–n heterojunction and GBs. Moreover, APT investigations revealed very distinct absorber surface compositions close to the p–n heterojunction when comparing the Cu-rich and Cu-poor cells. Strong Se enrichment is accompanied by a strong In depletion (down to 0 at% of In) as well as a little Cd enrichment at the CIGS surface of the Cu-rich cell, whereas strong Cu depletion is accompanied by Cd penetration at the CIGS surface (Cd_{Cu} defects) at the CIGS absorber surface of the Cu-poor CIGS cell. Device simulations confirmed that the presence of acceptor defects at the CIGS surface of a Cu-rich cell drastically impact the cell parameters. However, considering only the recombination coming from the p–n heterojunction could not reproduce the experimental findings, which suggested that the GBs have a role to play as well. Correlative EBIC-EBSD-APT measurements were performed on both samples and convincingly showed that all Cu-rich GBs are electrically detrimental. In the Cu-poor CIGS cell, only a minor proportion (15%) of GBs were Cu-rich and hence electrically detrimental. In the Cu-rich CIGS cell, all GBs were found to be electrically detrimental and enriched with Cu. DFT calculations showed that the superior properties of Cu-poor GBs are due to their efficient charge transfer behavior. In contrast, Cu-rich GBs entail deep gap states, not completely vanished by decorating the Cu-rich GBs with Na, which are active recombination centers. Device simulation further evidenced that the Cu-rich GBs determined electrically detrimental by EBIC are also detrimental for the cell performance, especially for the V_{OC}, whereas the Cu-poor GBs have only a minor negative impact on the cell efficiency.

Finally, typical fingerprints for superior properties of internal interfaces have been discovered. These are the Cu-depleted and Cd-enriched CIGS absorber surface near the p–n junction region as well as the negative Cu factor ($\Delta\beta$) and high Na content (>1.5 at%) at the GBs. Hence, this work provides key factors governing the device performance/efficiency and can be employed for the design of next-generation solar cells. Last but not least, this work is of great importance for material science given that GBs play a pivotal role in "GB engineering."

4. Experimental Section

CIGS Solar Cell Preparation: P-type CIGS layers with 2 µm thickness were deposited on Mo-coated soda-lime glass substrates at high temperatures in a three-stage co-evaporation process. The Cu-poor sample was prepared in a standard three-stage process. For preparation of the Cu-rich sample, the CIGS growth was stopped shortly after the endpoint detection to ensure formation of a copper-selenide phase on top the CIGS layer. After the growth, a KCN etching was performed to remove the excess copper-selenide phase ($Cu_{2-x}Se$) from the absorber surface.[50] Both samples were then completed to solar cells using similar processes. A CdS buffer layer (n-type) with a thickness of about 60 nm was deposited by chemical bath deposition. Then, an intrinsic ZnO layer (about 80 nm) was deposited by RF sputtering followed by DC sputtering of a front window layer of ZnO:Al (about 350 nm). Ni/Al/Ni contact grids for charge-carrier collection were deposited by electron beam evaporation through a shadow mask on top for charge carrier collection. Finally, cell separation for *I–V* measurements was done by mechanical scribing (total cell area of ≈0.5 cm^2).

The Cu-rich sample had a CGI ([Cu]/([In] + [Ga]) value of 1.13 and of 0.95 before and after KCN etching, respectively, and a constant GGI ([Ga]/([Ga] + [In]) value of 0.32. The Cu-poor cell had a CGI value of 0.83 and GGI value of 0.31. Although post-deposition treatments (PDTs) would have improved the efficiency as reported in our previous works,[9,34] the samples were not subjected to PDT in order to separate the effects of PDT which might overlap with effects of Cu content. Na was supplied only by outdiffusion of Na from the glass substrate during the CIGS process.

Experimental and Theoretical Investigations: Current–voltage (*I–V*) measurements were performed under illumination with AM1.5G simulated spectrum at standard test conditions. The CIGS composition and layer thickness were measured independently by X-ray fluorescence spectrometry (XRF) with an EAGLE XXL instrument from EDAX/Roentgenanalytik. For analysis, an Rh X-ray source was used, operating at 50 keV with an aperture of 1 mm diameter.

Samples for EBIC measurements were prepared by polishing and cleaning the samples with a dual-beam focused ion beam (FIB) scanning electron microscope (SEM), installed in FEI Helios NanoLab 650. The transfer of samples for EBIC measurements was immediate in order to avoid surface oxidation. A smart EBIC holder by Gatan Inc. was used for EBIC data acquisition and analysis in the same SEM/FIB setup. All EBIC measurements were performed in the dark without any external bias at room temperature. A gain of 5×10^5 and dwell time of 40 µs was used for quantitative data acquisition. For flattening the surface, the thin films were placed normal to the FIB source and the cross sections were polished (16 kV) and subsequently cleaned at low-energy ion beam (5 kV), leading to a high-quality surface (Ga-free and non-amorphized).

EBSD analysis was also performed in the same SEM/FIB setup, with the installed detector from EDAX using a DigiView 5 camera. EBSD measurements were performed on the identical regions of EBIC acquisition after complete EBIC analysis in order to avoid electron beam-induced damages on the surfaces. EBSD was performed at 20 kV and 1.6 nA SEM conditions using 4×4 binning resolution and step size of 50 nm. Data from EBSD results were processed using OIM data analysis software.

The sample fabrication steps for the correlative EBIC-EBSD-APT measurements could be found in Raghuwanshi et al.[18] APT analysis was conducted using a CAMECA LEAP-4000 Si (local electrode atom probe). For APT measurements, the specimen was maintained at 50 K and laser pulses (wavelength 355 nm) of 5 pJ energy were used for field evaporation. Detection rate of 1 ion per 500 pulses was chosen to obtain a 250 kHz pulse repetition rate.

Electronic structure calculations were performed in the framework of DFT using the projector augmented wave method as implemented in the Vienna Ab initio Simulation Package (VASP).[51–53] The plane-wave cutoff energy was set to 350 eV. Hubbard-corrected DFT calculations with a Hubbard on-site interaction parameter of $U = 5.0$ eV applied to the Cu 3d orbitals were performed for geometry optimization calculations.[54]

Supercells containing GBs were generated from the optimized bulk structure. To decouple a system with its periodic images, at least 30 Å of vacuum space was added along the *z*-axis. The atomic positions of the outer four layers were kept fixed at their bulk positions to mimic the bulk. All other atoms were allowed to relax during the geometry optimization. The atomic structures were considered to be optimized when the residual force on each atom was less than 0.1 eV $Å^{-1}$. The surface dangling bonds were passivated with hydrogen-like pseudoatoms.[55] A *k*-point mesh of $10 \times 4 \times 1$was used for the Brillouin zone integration. The Heyd–Scuseria–Ernzerhof screened-exchange hybrid functional,[55] was used for electronic structure calculations. The relative shift of the band edges was calculated by aligning the average electrostatic potentials in the bulk-like region far from GBs.[56] Atomic structures were visualized with VESTA.[57]

Numerical simulations of the solar cell were performed with the Synopsys Sentaurus TCAD suite, which solved the Poisson's equation coupled with the continuity equations for electrons and holes as well as the drift-diffusion transport equation. Nonradiative recombinations were obtained from the Shockley–Read–Hall statistics by defining the defect properties (acceptor/donor type, density, energy level, and capture cross-section) in the CIGS grain, at the GB, and in the remaining layers. The transfer matrix method optical solver was used to calculate the optical

generation under a standard AM1.5G solar spectrum, using wavelength-dependent complex refractive indexes.

The cell model had 3D cylindrical symmetry, with a grain of 750 µm radius surrounded by a 2 nm-thick GB, as described in Sozzi et al.[58] The cell featured the standard stack made of Al-doped ZnO (150 nm; n-type, 4×10^{19} cm^{-3}), highly resistive i-ZnO window (100 nm; n-type, 10^{17} cm^{-3}), CdS buffer (40 nm; n-type, 10^{17} cm^{-3}), and CIGS absorber (2 µm; p-type, 8×10^{15} cm^{-3}). Additional details on the simulations and parameters of different layers can be found in Sozzi et al.[59]

In the case of Cu-rich CIGS, recombinations at the p–n junction were simulated by considering a 5 nm-thick defective layer at the CIGS surface decorated with acceptor-like defects localized at $E_T - E_v = 0.2$ eV and due to a Se-related defect.[14]

Concerning GBs, two scenarios were examined: i) in Cu-poor cells, the GB (GI) was decorated with donor-like traps with concentration of 5×10^{18} (3.5×10^{15}) cm^{-3}, activation energy $E_c - E_T = 0.05$ eV, and electron/hole capture cross sections $\sigma_e/\sigma_h = 10^{-16}/1.1 \times 10^{-12}$ cm^2, and corresponding to In_{Cu} defects; and ii) in Cu-rich cells, the GB (GI) had acceptor-like defects corresponding to Cu_{In}/Cu_{Ga} defects with concentration of 5×10^{18} (1×10^{14}) cm^{-3}, localized at $E_T - E_v = 0.1$ eV and $E_T - E_v = 0.6$ eV and with electron/hole capture cross sections $\sigma_e/\sigma_h = 10^{-13}/1.3 \times 10^{-14}$ cm^2 and $\sigma_e/\sigma_h = 4 \times 10^{-15}/10^{-14}$ cm^2, respectively.

Supporting Information

Supporting Information is available from the Wiley Online Library or from the author.

Acknowledgements

M.R. and O.C.M. immensely acknowledge funding received from the Federal Ministry of Education and Research in Germany (BMBF 03×5522A) and the Federal Ministry for Economic Affairs and Climate Action (BMWK EFFCIS II, 03EE1059F) for fulfillment of this work. R.W. gratefully acknowledges funding of this work by the Projektträger Karlsruhe Baden-Württemberg Programme (SOLAMO project L75 16013). M.C., T.D.K., and H.M., acknowledge the Paderborn Center for Parallel Computing (PC2) for providing computing time on the FPGA-based supercomputer NOCTUA. The authors also gratefully acknowledge the Gauss Centre for Supercomputing e.V. (www.gauss-centre.eu) for funding this project by providing computing time on the GCS supercomputer JUWELS at Jülich Supercomputing Centre (JSC).

Open access funding enabled and organized by Projekt DEAL.

Conflict of Interest

The authors declare no conflict of interest.

Data Availability Statement

The data that support the findings of this study are available from the corresponding author upon reasonable request.

Keywords

Cu-poor Cu(In,Ga)Se_2, Cu-rich Cu(In,Ga)Se_2, device simulations, grain boundaries, p–n junctions, CIGS solar cells

Received: May 2, 2022
Revised: July 13, 2022
Published online: August 17, 2022

[1] M. Nakamura, K. Yamaguchi, Y. Kimoto, Y. Yasaki, T. Kato, H. Sugimoto, *IEEE J. Photovoltaics* **2019**, *9*, 1863.
[2] A. Gabor, J. Tuttle, M. Bode, A. Franz, A. Tennant, M. Contreras, R. Noufi, D. Jensen, A. Hermann, *Sol. Energy Mater. Sol. Cells* **1996**, *41–42*, 247.
[3] O. Lundberg, M. Edoff, L. Stolt, *Thin Solid Films* **2005**, *480–481*, 520.
[4] A. Chirilă, P. Reinhard, F. Pianezzi, P. Bloesch, A. R. Uhl, C. Fella, L. Kranz, D. Keller, C. Gretener, H. Hagendorfer, D. Jaeger, R. Erni, S. Nishiwaki, S. Buecheler, A. N. Tiwari, *Nat. Mater.* **2013**, *12*, 1107.
[5] P. Jackson, D. Hariskos, E. Lotter, S. Paetel, R. Wuerz, R. Menner, W. Wischmann, M. Powalla, *Prog. Photovoltaics* **2011**, *19*, 894.
[6] C. Beilharz, *Charakterisierung von aus der Schmelze gezuchteten Kristallen in den Systemen ¨Kupfer-Indium-Selen und Kupfer-Indium-Gallium-Selen fur photovoltaische Anwendungen*, Shaker Verlag, Düren, Germany **1999**.
[7] S. B. Zhang, S.-H. Wei, A. Zunger, *Phys. Rev. Lett.* **1997**, *78*, 4059.
[8] S. Siebentritt, L. Gütay, D. Regesch, Y. Aida, V. R. Deprédurand, *Sol. Energy Mater. Sol. Cells* **2013**, *119*, 18.
[9] P. Jackson, R. Wuerz, D. Hariskos, E. Lotter, W. Witte, M. Powalla, *Phys. Status Solidi* **2016**, *10*, 583.
[10] P. Jackson, D. Hariskos, R. Wuerz, O. Kiowski, A. Bauer, T. M. Friedlmeier, M. Powalla, *Phys. Status Solidi RRL* **2015**, *9*, 28.
[11] I. Repins, M. Contreras, M. Romero, Y. Yan, W. Metzger, J. Li, S. Johnston, B. Egaas, C. DeHart, J. Scharf, B. E. McCandless, R. Noufi, in *2008 33rd IEEE Photovoltaic Specialists Conf.*, IEEE, Piscataway, NJ, USA **2008**.
[12] V. R. Deprédurand, D. Tanaka, Y. Aida, M. Carlberg, N. Fèvre, S. Siebentritt, *J. Appl. Phys.* **2014**, *115*, 044503.
[13] Y. Aida, V. R. Depredurand, J. K. Larsen, H. Arai, D. Tanaka, M. Kurihara, S. Siebentritt, *Prog. Photovoltaics* **2015**, *23*, 754.
[14] H. Elanzeery, M. Melchiorre, M. Sood, F. Babbe, F. Werner, G. Brammertz, S. Siebentritt, *Phys. Rev. Mater.* **2019**, *3*, 055403.
[15] J. H. Werner, J. Mattheis, U. Rau, *Thin Solid Films* **2005**, *480–481*, 399.
[16] M. Turcu, O. Pakma, U. Rau, *Appl. Phys. Lett.* **2002**, *80*, 2598.
[17] V. Depredurand, Y. Aida, J. Larsen, T. Eisenbarth, A. Majerus, S. Siebentritt, in *2011 37th IEEE Photovoltaic Specialists Conf.*, IEEE, Piscataway, NJ, USA **2011**, pp. 000337–000342.
[18] M. Raghuwanshi, R. Wuerz, O. Cojocaru-Mirédin, *Adv. Funct. Mater.* **2020**, *30*, 2001046.
[19] O. Cojocaru-Mirédin, M. Raghuwanshi, R. Wuerz, S. Sadewasser, *Adv. Funct. Mater.* **2021**, *31*, 2103119.
[20] N. Nicoara, R. Manaligod, P. Jackson, D. Hariskos, W. Witte, G. Sozzi, R. Menozzi, S. Sadewasser, *Nat. Commun.* **2019**, *10*, 3980.
[21] M. Krause, A. Nikolaeva, M. Maiberg, P. Jackson, D. Hariskos, W. Witte, J. A. Márquez, S. Levcenko, T. Unold, R. Scheer, D. Abou-Ras, *Nat. Commun.* **2020**, *11*, 4189.
[22] S. Siebentritt, E. Avancini, M. Bär, J. Bombsch, E. Bourgeois, S. Buecheler, R. Carron, C. Castro, S. Duguay, R. Félix, E. Handick, D. Hariskos, V. Havu, P. Jackson, H.-P. Komsa, T. Kunze, M. Malitckaya, R. Menozzi, M. Nesladek, N. Nicoara, M. Puska, M. Raghuwanshi, P. Pareige, S. Sadewasser, G. Sozzi, A. N. Tiwari, S. Ueda, A. Vilalta-Clemente, T. P. Weiss, F. Werner, et al., *Adv. Energy Mater.* **2020**, *10*, 1903752.
[23] M. Kawamura, T. Yamada, N. Suyama, A. Yamada, M. Konagai, *Jpn. J. Appl. Phys.* **2010**, *49*, 062301.
[24] G. Hanna, T. Glatzel, S. Sadewasser, N. Ott, H. P. Strunk, U. Rau, J. H. Werner, *Appl. Phys. A* **2006**, *82*, 1.
[25] C.-S. Jiang, R. Noufi, J. A. Abushama, K. Ramanathan, H. R. Moutinho, J. Pankow, M. M. Al-Jassim, *Appl. Phys. Lett.* **2004**, *84*, 3477.
[26] H. Mönig, R. Caballero, C. A. Kaufmann, T. L. Schmidt, M. C.h. Lux-Steiner, S. Sadewasser, *Sol. Energy Mater. Sol. Cells* **2011**, *95*, 1537.
[27] S. B. Zhang, S.u-H. Wei, A. Zunger, H. Katayama-Yoshida, *Phys. Rev. B* **1998**, *57*, 9642.

[28] F. Couzinie-Devy, E. Cadel, N. Barreau, L. Arzel, P. Pareige, *Appl. Phys. Lett.* **2011**, *99*, 232108.
[29] B. Gault, A. Chiaramonti, O. Cojocaru-Mirédin, P. Stender, R. Dubosq, C. Freysoldt, S. K. Makineni, T. Li, M. Moody, J. M. Cairney, *Nat. Rev. Methods Primers* **2021**, *1*, 51.
[30] O. Cojocaru-Mirédin, A. Devaraj, *MRS Bull.* **2022**, https://doi.org/10.1557/s43577-022-00369-4.
[31] J. Keutgen, A. J. London, O. Cojocaru-Mirédin, *Microsc. Microanal.* **2021**, *27*, 28.
[32] O. Cojocaru-Mirédin, P. Choi, R. Wuerz, D. Raabe, *Appl. Phys. Lett.* **2011**, *98*, 103504.
[33] O. Cojocaru-Mirédin, P. Choi, R. Wuerz, D. Raabe, *Appl. Phys. Lett.* **2012**, *101*, 181603.
[34] M. Raghuwanshi, A. Vilalta-Clemente, C. Castro, S. Duguay, E. Cadel, P. Jackson, D. Hariskos, W. Witte, P. Pareige, *Nano Energy* **2019**, *60*, 103.
[35] Z.-K. Yuan, S. Chen, Y. Xie, J.-S. Park, H. Xiang, X.-G. Gong, S.-H. Wei, *Adv. Energy Mater.* **2016**, *6*, 1601191.
[36] J. D. Poplawsky, N. R. Paudel, C. Li, C. M. Parish, D. Leonard, Y. Yan, S. J. Pennycook, *Adv. Energy Mater.* **2014**, *4*, 1400454.
[37] C. Li, Y. Wu, J. Poplawsky, T. J. Pennycook, N. Paudel, W. Yin, S. J. Haigh, M. P. Oxley, A. R. Lupini, M. Al-Jassim, S. J. Pennycook, Y. Yan, *Phys. Rev. Lett.* **2014**, *112*, 156103.
[38] C. P. Muzzillo, J. D. Poplawsky, H. M. Tong, W. Guo, T. Anderson, *Prog. Photovoltaics* **2018**, *26*, 825.
[39] M. Raghuwanshi, B. Thöner, P. Soni, M. Wuttig, R. Wuerz, O. Cojocaru-Mirédin, *ACS Appl. Mater. Interfaces* **2018**, *10*, 14759.
[40] P.-P. Choi, O. Cojocaru-Mirédin, R. Wuerz, D. Raabe, *J. Appl. Phys.* **2011**, *110*, 124513.
[41] O. Cojocaru-Miredin, T. Schwarz, P.-P. Choi, M. Herbig, R. Wuerz, D. Raabe, *J. Visualized Exp.* **2013**, *74*, e50376.
[42] O. Cojocaru-Mirédin, P. Choi, R. Wuerz, D. Raabe, *Ultramicroscopy* **2011**, *111*, 552.
[43] A. Stokes, M. Al-Jassim, D. Diercks, A. Clarke, B. Gorman, *Sci. Rep.* **2017**, *7*, 14163.
[44] O. Cojocaru-Mirédin, T. Schwarz, D. Abou-Ras, *Scr. Mater.* **2018**, *148*, 106.
[45] B. Gaury, P. M. Haney, *Phys. Rev. Appl.* **2017**, *8*, 054026.
[46] T. Schwarz, G. Stechmann, B. Gault, O. Cojocaru-Mirédin, R. Wuerz, D. Raabe, *Prog. Photovoltaics* **2018**, *26*, 196.
[47] J. Pohl, K. Albe, *Phys. Rev. B* **2013**, *87*, 245203.
[48] M. Chugh, T. D. KÃ¼Hne, H. Mirhosseini, *ACS Appl. Mater. Interfaces* **2019**, *11*, 14821.
[49] S. Shukla, D. Adeleye, M. Sood, F. Ehre, A. Lomuscio, T. P. Weiss, D. Siopa, M. Melchiorre, S. Siebentritt, *Phys. Rev. Mater.* **2021**, *5*, 055403.
[50] R. Caballero, C. A. Kaufmann, V. Efimova, T. Rissom, V. Hoffmann, H. W. Schock, *Prog. Photovoltaics* **2013**, *21*, 30.
[51] P. E. Blöchl, *Phys. Rev. B: Condens. Matter Mater. Phys.* **1994**, *50*, 17953.
[52] G. Kresse, J. Hafner, *Phys. Rev. B* **1993**, *47*, 558.
[53] G. Kresse, D. Joubert, *Phys. Rev. B* **1999**, *59*, 1758.
[54] S. L. Dudarev, G. A. Botton, S. Y. Savrasov, C. J. Humphreys, A. P. Sutton, *Phys. Rev. B* **1998**, *57*, 1505.
[55] K. Shiraishi, *J. Phys. Soc. Jpn.* **1990**, *59*, 3455.
[56] H.-P. Komsa, T. T. Rantala, A. Pasquarello, *Phys. Rev. B* **2012**, *86*, 045112.
[57] K. Momma, F. Izumi, *J. Appl. Crystallogr.* **2011**, *44*, 1272.
[58] G. Sozzi, O. Cojocaru-Mirédin, R. Wuerz, *2021 IEEE 48th Photovoltaic Specialists Conf. (PVSC)*, IEEE, Piscataway, NJ, USA **2021**, pp. 0187–0191.
[59] G. Sozzi, R. Menozzi, *2020 47th IEEE Photovoltaic Specialists Conf. (PVSC)*, IEEE, Piscataway, NJ, USA **2020**, pp. 1145–1148.